TWO AND THREE-DIMENSIONAL SHOCK-SHOCK INTERACTIONS ON THE BLUNT LEADING EDGES OF THE HYPERSONIC INLETS

D. J. Singh*
Old Dominion University
Norfolk, VA

A. Kumar†
NASA Langley Research Center
Hampton, VA

S. N. Tiwari‡
Old Dominion University
Norfolk, VA

ABSTRACT

The effect of shock impingement on the blunt leading edges of the top and the sidewall compression type inlet of a scramjet engine is investigated numerically. The impinging shock is caused by the vehicle forebody. The interaction of this forebody shock with the inlet leading edge shock results in a very complex flowfield containing local regions of high pressure and intense heating. In the present investigation, this complex flowfield is calculated by solving the Navier-Stokes equations using a finite-volume flux splitting technique due to van Leer. To resolve the finer details of the flow structure as well as to predict the surface heat transfer accurately, adaptive grid technique is used in the analysis. Results of the present numerical investigation are compared with available experimental results.

NOMENCLATURE

a	= speed of sound
e	= total energy per unit volume
E, F, G	= inviscid fluxes
E_v, F_v, G_v	= viscous flux
J	= transformation Jacobian
k	= coefficient of thermal conductivity
M	= Mach number
Pr	= Prandtl number
P	= pressure
Q	= Conserved Variables
q	= heat transfer

*Graduate Research Assistant, Department of Mechanical Engineering and Mechanics.
Present Affiliation: Analytical Systems and Material Inc., Hampton, VA.
†Head, Theoretical Flow Physics Branch, Fluid Mechanics Division.
‡Eminent Professor, Department of Mechanical Engineering and Mechanics.

Re = Reynolds number
Rn = nose radius
t = time
T = temperature
γ = ratio of specific heats
δ = shock angle
θ = angular position on the body
Λ = sweep angle
ξ, η, ζ = curvilinear coordinates
ρ = density
τ = viscous shear stress

Subscripts

aw = adiabatic wall
D = diameter
s = stagnation line conditions
w = wall conditions
∞ = freestream conditions

INTRODUCTION

In order to properly design the high speed inlets, it is necessary to perform a detailed flowfield analysis under all plausible circumstances. One of the concerns in the inlet design is the possibility of forebody shock interaction with the shocks generated by the blunt leading edges of the inlet compression surfaces (Fig. 1). These interactions cause a very complex flowfield and can result in large increase in pressure and heat transfer over a local region. The large temperature gradients cause thermal stresses which could result in structural failure. In order to relieve the influence of thermal stresses, some form of active cooling is needed. To determine the cooling requirements, pressure and heating rates on the body need to be predicted accurately.

In the present investigation, the interaction of forebody shock with the top wall and the swept sidewall compression inlets is studied. The effect of shock impingement on the cowl of a topwall compression inlet is investigated first. This kind of interaction can be studied using a two-dimensional analysis. The use of full Navier Stokes equations with the solution adaptive grid is made to calculate the flow field. The sidewall compression inlets are investigated next. These inlets have swept back sidewalls to allow for flow spillage. The interaction of forebody shock with the inlet sidewalls produces a fully three-dimensional flowfield due to orientation of the impinging shock as well as sweep of the inlet sidewalls. The three-dimensional thin-layer Navier-Stokes equations are used to calculate this interaction. The cowl and the inlet sidewalls are modeled by two-and three-dimensional blunt wedges respectively. The forebody shock is modeled by a planar shock generated by a sharp wedge. The physical models used to study the shock - shock interactions on the topwall and the sidewall compression inlets are shown in Figs. 2 and 3, respectively.

Edney [1] was the first to study the interaction effects experimentally. He described six types of interaction patterns depending upon the location and strength of the impinging shock. Keyes and Hains [2] continued the work of Edney for higher Mach numbers and a wide range of Reynolds number. Several investigators [3] - [15] have studied the two-dimensional shock-shock

interaction on the cowl leading edge. Wieting [3]conducted an experimental study on the shock wave interference over a cylindrical leading edge at Mach 6.3, 6.5 and 8.0. Several semi-empirical approaches have been proposed to theoretically predict the peak heating and pressure (Refs. [4] - [8]) but they rely on several empirical inputs such as the length of transmitted shock which must be known apriori. There are very few numerical studies available due to the complexity of the problem. Tannehill et al. [9,10] presented the first successful numerical simulation of the interaction problem based on the explicit MacCormack method. White [11] solved this problem using the Reynolds-averaged Navier-Stokes equations (based on an implicit finite-volume method) and obtained results for Mach 6.0. Klopfer [12] conducted an extensive study for various Mach numbers using the second-order implicit TVD algorithm. Perry et al. [13] used the Roe scheme to solve the Type IV interactions but did not give any heat transfer results. Moon [14] provided the results for the Type III interference pattern. The study indicated that the flow for this type of interaction in the impingement region is turbulent rather than laminar. Singh et al. [15] solved the flow around complete cowl lip including the downstream effects of shock-shock interactions into the inlet. van Leer's flux vector splitting technique was used to solve the Navier-Stokes equations on the cowl forebody and the parabolized Navier-Stokes equations on the cowl afterbody. In order to properly resolve the gradients, the adaptive grids were used.

The first systematic study of shock interaction heating in supersonic flows up to Mach 5.5 on swept and unswept fins was conducted by Newlander [16] and Carter and Carr [17]. These studies showed the heating enhancements up to 10 times the stagnation line heating for unimpinged case. Beckwith [18] and Bushnell [19] measured the heating rates on a swept cylinder close to its junction with a wedge. Glass et al. [20] investigated the effects of cowl sweep by creating a quasi-two-dimensional flow by sweeping the interaction zone. The axis of impinging shock was aligned parallel to the axis of the cylinder similar to the two-dimensional case [3]. Due to sweep, the component of flow normal to the body decreases and hence the peak values of pressure and heat transfer decrease. Holst et al. [21] conducted the first numerical simulation of full three-dimensional shock-shock interaction problem on an infinite cylinder using the explicit MacCormack scheme. The viscosity was assumed to be an order of magnitude higher than normal to physically thicken the boundary layer. A very coarse grid of 21x21x41 was employed. It gave the first insight of the difficulties associated with numerical simulation of such a complex flow. Due to coarseness of the grid and the assumption of higher viscosity, the resulting solution was at best qualitative in nature. The end effects of the inlet/body junction are neglected and the inlet sidewall is modeled by a wedge with 5^0 compression angle. The sweep angle is 25^0 for Type V interaction and the impinging shock is generated by a sharp wedge. Results of the present investigation are compared with the available experimental results.

GOVERNING EQUATIONS AND COMPUTATIONAL PROCEDURES

The three-dimensional Navier-Stokes equations in fully conservative form can be written in the generalized coordinates as

$$\frac{\partial \hat{Q}}{\partial t} + \frac{\partial(\hat{E} - \hat{E}_v)}{\partial \xi} + \frac{\partial(\hat{F} - \hat{F}_v)}{\partial \eta} + \frac{\partial(\hat{G} - \hat{G}_v)}{\partial \zeta} = 0 \tag{1}$$

The inviscid and viscous flux vectors in generalized coordinate system are defined as

$$\hat{Q} = \frac{1}{J}\begin{bmatrix} \rho \\ \rho u \\ \rho v \\ \rho w \\ e \end{bmatrix}, \quad \hat{E} = \frac{1}{J}\begin{bmatrix} \rho U \\ \rho U u + \xi_x p \\ \rho U v + \xi_y p \\ \rho U w + \xi_z p \\ (e+p)U \end{bmatrix}, \quad E_v = \frac{1}{J}\begin{bmatrix} 0 \\ \xi_x \tau_{xx} + \xi_y \tau_{xy} + \xi_z \tau_{xz} \\ \xi_x \tau_{yx} + \xi_y \tau_{yy} + \xi_z \tau_{yz} \\ \xi_x \tau_{zx} + \xi_y \tau_{zy} + \xi_z \tau_{zz} \\ \xi_x b_x + \xi_y b_x + \xi_z b_z \end{bmatrix}$$

$$\hat{F} = \frac{1}{J}\begin{bmatrix} \rho V \\ \rho V u + \eta_x p \\ \rho V v + \eta_y p \\ \rho V w + \eta_z p \\ (e+p)V \end{bmatrix}, \quad F_v = \frac{1}{J}\begin{bmatrix} 0 \\ \eta_x \tau_{xx} + \eta_y \tau_{xy} + \eta_z \tau_{xz} \\ \eta_x \tau_{yx} + \eta_y \tau_{yy} + \eta_z \tau_{yz} \\ \eta_x \tau_{zx} + \eta_y \tau_{zy} + \eta_z \tau_{zz} \\ \eta_x b_x + \eta_y b_x + \eta_z b_z \end{bmatrix}$$

$$\hat{G} = \frac{1}{J}\begin{bmatrix} \rho W \\ \rho W u + \varsigma_x p \\ \rho W v + \varsigma_y p \\ \rho W w + \varsigma_z p \\ (e+p)W \end{bmatrix}, \quad G_v = \frac{1}{J}\begin{bmatrix} 0 \\ \varsigma_x \tau_{xx} + \varsigma_y \tau_{xy} + \varsigma_z \tau_{xz} \\ \varsigma_x \tau_{yx} + \varsigma_y \tau_{yy} + \varsigma_z \tau_{yz} \\ \varsigma_x \tau_{zx} + \varsigma_y \tau_{zy} + \varsigma_z \tau_{zz} \\ \varsigma_x b_x + \varsigma_y b_x + \varsigma_z b_z \end{bmatrix}$$

where U, V, and W are contravarient velocities and are given as,

$$U = \xi_x u + \xi_y v + \xi_z w$$
$$V = \eta_x u + \eta_y v + \eta_z w$$
$$W = \varsigma_x u + \varsigma_y v + \varsigma_z w$$

and

$$b_{x_i} = u_j \tau_{x_i x_j} - \dot{q}_{x_i} \tag{2}$$

The cartesian velocity components are u, v, and w in the x, y, and z directions, respectively. The pressure p is related to the conserved variables through the ideal gas law

$$p = (\gamma - 1)[e - \rho(u^2 + v^2 + w^2)/2] \tag{3}$$

The equations are nondimensionalized in terms of freestream density and speed of sound. The chain rule is used to evaluate the derivatives with respect to (x,y) in terms of (η, ς). The cell volume is 1/J and the surface area of the cell in the η direction is $|\Delta\eta|$/J. The Stokes hypothesis, $\lambda = -\frac{2}{3}\mu$, is used for the bulk viscosity, and the viscosity is evaluated by using the Sutherland's law. The equations were suitably modified for two-dimensional analysis and are given in Ref. [15]. Also, for the three-dimensional analysis the viscous terms in streamwise and crossflow directions (E_v and F_v) were dropped to obtain the thin-layer Navier-Stokes equations.

An implicit, second-order accurate, upwind biased finite-volume scheme developed by Thomas et al. [22] is used to solve the Navier-Stokes equations. The flux vector splitting of van Leer is used for the inviscid part and the viscous terms are centrally differenced. The method is second order accurate in space and first order accurate in time. Beam and Warming [23] type approximate factorization is used to solve the system of equations in two sweeps. The algorithm is described in Refs. [22] and [24].

The wall pressure and heat transfer are nondimensionalized with respect to the unimpinged stagnation point(line) values. For two-dimensional calculations, the unimpinged stagnation values were calculated numerically while for the three-dimensional case they were obtained by approximate correlations in order to be consistent with Ref. [2]. The unimpinged stagnation line pressure is obtained by the Rayleigh-pitot formula as

$$\frac{p_s}{p_\infty} = \left(\frac{6M_1^2}{5}\right)^{\frac{7}{2}}\left(\frac{6}{7M_1^2 - 1}\right)^{\frac{5}{2}} \tag{4}$$

where M_1 is the normal Mach number. The stagnation line heat transfer is obtained by the following expression developed by Beckwith and Gallagher [18]

$$q_s = k_\infty \frac{T_{aw} - T_w}{2D}\left(\frac{2Re_{D,\infty}\mu_s}{M_\infty \mu_\infty}\right)^{\frac{1}{2}}\left[\frac{2T_\infty p_s}{\gamma T_s p_\infty}\left(\frac{p_s}{p_\infty} - 1\right)\right]^{\frac{1}{4}} \tag{5}$$

where

$$T_{aw} = T_e(1 + r\frac{\gamma - 1}{2}M_e^2)$$

here r is the recovery factor and is taken as 0.85 and subscript e denotes the boundary layer edge conditions.

The inflow boundary is divided into two parts: freestream conditions are maintained at all grid points above the impingement point (line). For all points below the impingement point (line), the conditions are calculated by Rankine-Hugoniot relations for the given freestream Mach number and the impinging shock angle. The outflow conditions are obtained by first order extrapolation. Along the wall, zero slip, isothermal wall, and zero pressure gradient conditions are imposed.

GRID

The first step in any numerical solution is the discretization of the governing equations from continuous domain to a set of discrete points. The choice of grid points is not an arbitrary one but is governed by the physics of the problem. Since the computer memory and speed limits the number of grid points, it is very crucial to make best use of the available resources. The grid points should conform to the boundaries and be concentrated in the regions of high gradients, such as shocks, boundary layer etc., in order to properly resolve the flow field. They must also be oriented in such a way that the grid is as nearly orthogonal as possible. Since the shock capturing algorithm was employed, the outer boundary was chosen in such a way that there were sufficient number of points between the shock and the outer boundary. The grid points were clustered normal to the body using the exponential stretching. Since heat transfer and skin friction coefficients are very strong function of grid spacing, it is very important to properly resolve the gradients. For impingement case, the distorted bow shock moves closer to the body on one side and away on the other side; thus a large number of grid points is wasted. Near the impingement point, the grid is too coarse to capture finer details of the flow. To alleviate this problem, an adaptive grid system was employed which adapts the grids during the course of the solution in order to follow the developing gradients in the physical solution. The grid points move as the solution develops, concentrating the points where they are needed the most. The total number of points were kept constant. For this, the method developed by Abolhassani et al. [25] was used. It is a very general method with capability to adapt the grids with various variables such as pressure, Mach number, shear stress etc. and is based on variational approach. It is an algebraic method and is formulated in such a way that there is no need for matrix inversion, which makes it computationally very efficient. Since the solution varies predominantly in normal direction, the grid is adapted in only one direction.

RESULTS AND DISCUSSION

The numerical scheme discussed previously has been used to compute the two-and three-dimensional shock-shock interactions on the inlet leading edge of a scramjet engine. As mentioned earlier, only Type IV interaction is considered for the topwall compression inlet since it is the most severe case in terms of pressure and heating rates on the surface. The freestream conditions used are given in Table 1; these were selected due to the availability of the experimental data. The results for the two-dimensional case are discussed first, followed by the three-dimensional results. For all cases, the undisturbed blunt body flow was calculated first and this solution was then used as initial condition for shock impingement calculations.

A schematic of the Type IV interaction is shown in Fig. 4. This type of interaction occurs when the impinging shock strikes the leading edge shock (bow shock) near the stagnation zone, where the shock is nearly normal. This produces a supersonic jet bounded by two shear layers and submerged in subsonic flow. Near the body, it produces jet bow shock and stagnation zone when it strikes the body. This produces a very complex flow field with presence of shocks, shear layers

and the jet. Type IV interaction is the most severe case and produces the largest amplification of heating and pressure.

Figure 5 shows the grid used to compute the cowl forebody flowfield. The outer boundary of the computational domain has been adapted to the distorted bow shock, which was obtained by coarse mesh calculations. Since the shock capturing algorithm has been used, the outer boundary was moved far enough to avoid shock interaction with the outer boundary. Due to poor comparison of heating rates and smearing of important flow features, [15], it was decided to use adaptive grids thereby placing the grid points where they are needed the most. Body curvature, pressure and density were chosen as weight functions to adapt the grid to the solution. The body curvature clusters the grid points very close to the body while pressure and density attract the grid points near shocks and shear layers. Thirty percent of the points were allocated for adaption by body curvature, forty percent by pressure and density and the rest were used for creating uniformity of the grid so that the grid is not too coarse in any section.

Temperature and Mach number contours are shown in Figs. 6 and 7, respectively. The distorted bow shock is clearly evident in the figures. The bow shock has moved toward the body on the windward side and away from it on the leeward side. Here windward side is defined as the upper side where the flow passes through the impinging shock before encountering the body. The interaction of the bow shock and the impinging shock produces a supersonic jet surrounded by subsonic flow. The jet terminates with jet shocks and impinges on the body producing a local zone of very high pressure and heating rates. The stagnation point moves towards the windward side. The location of the stagnation point depends upon the strength and orientation of the impinging shock. Since the grid is fine near the shocks and shear layer, the flow features are captured very well. The location of the stagnation point, jet and shear layer orignating from the shock intersection can be seen clearly. The shear layer orignating from the stagnation zone is much thicker on the leeward side as compared to the windward side.

Figure 8 shows the velocity vectors for the cowl forebody flow. Even though the flow is at zero angle of attack, its direction is changed as it passes through the impinging shock. The shear layer on the leeward side is seen clearly orignating from the stagnation point which has moved (as compared to unimpinged case) toward the windward side.

The variation of wall pressure along the cowl forebody surface is shown in Fig. 9. The pressure is nondimensionalized by the stagnation point pressure for unimpinged blunt body flow. In order to properly visualize the effect of shock - shock interaction, the surface pressure for unimpinged blunt body flow for the same free stream conditions is also shown in the figure. The pressure on the windward side increases considerably with a localized zone of high pressure and falls below the surface pressure for unimpinged case on the leeward side. The peak value of pressure is about 9 times the stagnation point value. The results compare very well with the experimental data of Wieting [3] and numerical calculations of Klopfer [12]. It should be noted that for this case the location of the impinging shock was made to coincide with the experimental location by matching the peak pressure location.

Figure 10 shows the heat transfer along the wall on the cowl forebody. The heating rates are nondimensionalized with respect to the stagnation point heating for unimpinged case. It shows a similar behavior as the surface pressure, i.e., an increased heating on the windward side and decreased heating on the leeward side. A localized zone of intense heating is observed on the windward side. The heating rates show a remarkable improvement over the previous calculations. The results compare favorably with the experiment. The discrepancy in the peak is probably due to the unsteadiness in the flow and/or the turbulent nature of the jet as is indicated recently by Moon et al. [14]. For this case, the solution was found to be marginally unsteady as the residual did not go down more than three orders of magnitude. Also the jet oscillated slightly, thereby changing the location of the peak pressure and heating. A similar behaviour was noted for the Type IV interaction in Refs. [12] and [13].

Similar calculations were carried out for Mach 5.94 freestream conditions and the results

are shown in Figs. 11 and 12. Qualitatively these results are very similar to the Mach 8.03 conditions. The grid for this case is generated in the same way as for the previous case. The variations of surface pressure and heat transfer are shown in Figs 11 and 12 respectively. The numerical results are compared with the experimental data reported by Tannehill et al. [10] from an unpublished experiment by J. W. Keyes of NASA Langley. The computed values of surface pressure agree very well with the experimental data although the peak pressure is slightly lower than the experimental peak. Although not shown here, the peak value of the pressure matches with the numerical calculations of Tannehill et al. [10]. The variation of heat transfer on the cowl forebody is shown in Fig. 12. For heating rates, the experimental data was reported only at one point. The peak value of the heating is 6.4 times the stagnation point value, which is within the uncertainty range of the experiment.

Now, the results for sidewall compression type inlets will be discussed. As mentioned earlier, the shock-shock interaction on this type of inlet results in a fully three-dimensional flowfield. The results are presented for Type V interaction only. Calculations have been performed for Type IV interaction also [26] but the flowfield didn't converge to a steady state solution. Further investigation of this case is currently underway. The freestream conditions used for the present calculations are given in Table 1.

The schematic diagram of the Type V interference on the swept inlet sidewall is shown in Fig. 13. The interaction of the two shocks of unequal strength produces a lambda shock which divides the flow into two portions separated by a contact discontinuity that begins at the nodal point of the lambda shock. The two sides have the same pressure and the flow direction but different magnitude of velocities, temperature and density across this discontinuity. Due to sweep of the body, the component of flow normal to the body reduces and hence the strength of the intersecting shocks decreases. The peak heating and the pressure impingement occurs at the point where the shear layer impinges at the surface. The peak value depends on various factors such as the Mach number, impinging shock angle, and sweep of the body.

A grid of 29x49x61 has been used which is clustered near the wall and the impingment location to resolve the boundary layer and the shear layer as shown in Fig. 14. Since the flow is symmetric about the stagnation plane, only one half of the flow is considered. As in the previous case, the outer boundary was moved far enough so as to avoid any interference between the shock and the outer boundary. No attempt was made to adapt the grids to the solution.

Figure 15 shows the temperature, Mach number and pressure contours in the stagnation plane with shock impingement. The temperature contours are shown in Fig. 15(a). Due to stretching, the grid away from the surface is coarse; consequently, the shock and the other flow features are smeared over several grid points. The impinging shock is clearly visible in the figure. The bow shock moves away from its unimpinged position and a shear layer is produced. The shear layer interacts with the boundary layer. Also, a transmitted shock is produced which strikes the body causing a jump in pressure and heating rates. These are typical features of the Type V interaction. There are temperature and density gradients across the shear layer. The Mach number contours are shown in Fig. 15(b); the flow is supersonic behind the bow shock and the shear layer can also be seen. Figure 15(c) shows the pressure contours in the stagnation plane. Since the pressure is constant across the shear layer, it is not visible in this figure. Some expansion waves can be seen emanating from the intersection point which reduce the surface pressure as the flow expands.

Figure 16 (taken from Ref. [1]) shows a cylindrical fin coated with temperature sensitive paint and the corresponding schlieren photograph locating regions of high pressure and heat transfer for Type V interference. It should be noted that the freestream conditions for this case are slightly different but it shows a typical Type V interaction. The corresponding numerical solutions are shown in Figs. 17 and 18. The surface pressure contours are shown in Fig. 17 and the stagnation plane pressure contours in Fig. 18. The numerical solution captured the first two (A and B) peaks in pressure and heat transfer. The third peak (C), caused by the flow separation near the end, is absent in the numerical solution due to the assumption of infinite length of the body. The behavior of bow shock near the impingement point is very well captured by the numerical scheme.

The comparison of Figs. 16(b) and 18 shows how well the physical phenomenon is captured by the numerical scheme.

Figures 19 and 20 show the variation of pressure and heat transfer along the surface. They are nondimensionalized with respect to the unimpinged stagnation line values. Figure 19 shows the comparison of stagnation line pressure with the experimental data of Keyes and Hains [2] and numerical calculations of Holst et al. [21]. In the experimental set up, the interaction point was only 3 cm downstream from the end of the cylinder (z = 0) and, therefore, there was some relieving effect (Fig. 16). But in the present calculations, the body is assumed as infinite in length and hence no relieving effect is allowed. Due to this discrepancy, the results do not match near the end. However, the results compare fairly well away from the end point. The peak value of the pressure is caused by the interaction of the transmitted shock with the boundary layer and it is very well captured. The flow overexpands and then recompresses back to the unimpinged value. The peak value of the pressure is about 2.2 times the unimpinged stagnation line pressure. The variation of the stagnation line heat transfer is shown in Fig. 20. In this case also, the comparison is poor near the end for the same reasons as explained earlier. But away from the end, results compare fairly well. As expected, the heat transfer follows the same general trend as the pressure. The peak value of heat transfer is about three times the unimpinged stagnation line heat transfer. The experimental data is available only for the stagnation plane.

The results from the present calculations show a remarkable improvement over Holst's calculations due to various factors. The flow field is much better resolved due to a finer grid and no artificial thickening of the boundary layer has been imposed. Also, in Holst's calculations, the flow variables at the z=0 boundary were held fixed for all time equal to the unimpinged flow solution, which is incorrect for the impinging shock case.

CONCLUSIONS

The numerical scheme mentioned previously has been used to compute the two-and three-dimensional shock-shock interaction on the inlet walls of the scramjet engine. For the topwall compression inlet(two-dimensional model) the Type IV shock-shock interaction is investigated since it is the most severe one, producing maximum increase in pressure and heating rates. To resolve the finer details of the flow, adaptive grid technique has been used. All flow features were captured by the numerical calculations and the results compare very well with the experimental data. In the case of sidewall compression type inlet (three-dimensional model), the Type V interaction is studied. In this case also the results agree very well with the experimental data.

References

[1] Edney, B. E., " Anomalous Heat Transfer and Pressure Distribution on Blunt Bodies at Hypersonic speeds in the Presence of an Impinging Shock, " Aeronautical Research Institute of Sweden, FAA Report 115, February 1968.

[2] Keyes, J. W. and Hains, F. D., " Analytical and Experimental Studies of Shock Interference Heating in Supersonic Flows, " NASA TN D-7139, May 1973.

[3] Wieting, A. R. and Holden, M. S., " Experimental Study of Shock Wave Interference Heating in Supersonic Flows, " AIAA Paper 87-1511, June 1987.

[4] Morris, D. J. and Keyes, J. W., " Computer Programs for Predicting Supersonic and Hypersonic Interference Flowfield and Heating, " NASA TM X-2725, May 1973.

[5] Keyes, J. W.and Morris, D, J., " Correlations of Peak Heating in Shock Interference Regions at Hypersonic Speeds," Journal of Spacecraft and Rockets, Vol. 9, August 1972, pp. 621-623.

[6] Bramlette, T. T., " Simple Technique for Predicting Type III and IV Shock Interference, " AIAA Journal , Vol. 2, August 1974, pp. 1151-1152.

[7] Markarian, C. F., " Heat Transfer in Shock Wave Boundary layer Interactions, " Naval Weapons Center, China Lake, California, NWC TP 4485, November 1968.

[8] Bertin, J. J., Graumann, B. W., and Goodrich, W. D., " Analysis of High Velocity and Real Gas Effects on the Shock-Interference Pattern for Delta - Wing Orbiters, " AIAA Paper 74-522, June 1974.

[9] Tannehill, J. C., Holst, T. L., and Rakich, J. V., " Numerical Computation of a Two - Dimensional Viscous Blunt Body Flows with an Impinging Shock, " AIAA Journal, Vol. 14, No. 2, February 1976, pp. 204-211.

[10] Tannehill, J. C., Holst, T. L., Rakich, J. V., and Keyes, J. W., " Comparison of a Two - Dimensional Shock Impingement Computation With Experiment, " AIAA Journal, Vol. 14, April 1976, pp. 539-541.

[11] White, J. A. and Rhie, C. M., " Numerical Analysis of Peak Heat Transfer Rates for Hypersonic Flow Over a Cowl Leading Edge, " AIAA Paper 87-1895, June 1987.

[12] Klopfer, G. H. and Yee, H. C., " Viscous Hypersonic Shock-On-Shock Interaction on Blunt Cowl Lips, " AIAA Paper 88-0233, January 1988.

[13] Perry, K. M. and Imley, S. T., " Blunt Body Flow Simulations, " AIAA Paper 88-2904, July 1988.

[14] Moon, Y. J. and Holt, M.," Interaction of an Oblique Shock with Turbulent Hypersonic Blunt Body Flows, " AIAA Paper 89-0272, January 1989.

[15] Singh, D. J., Kumar, A., and, Tiwari, S. N.,"Influence of Shock - Shock Interaction on the Flow Field at Hypersonic Flight Speeds," AIAA 89-2184, July 1989.

[16] Newlander, R. D.," Effects of Shock Impingement on the Distribution of Heat Transfer Coefficient on a Right Circular Cylinder at Mach Number of 2.65, 3.51 and 4.44, " NASA TN D-642, 1961.

[17] Carter, H. S. and Carr, R. E., " Free Flight Investigation of Heat Transfer to an Unswept Cylinder Subjected to an Incident Shock and Flow Interference From an Upstream Body at Mach number up to 5.50," NASA TN D-9909.

[18] Beckwith, I. E., "Experimental Investigation of Heat Transfer and Pressure on a Swept Cylinder in the Vicinity of its Interaction with a Wedge and Flat Plate at Mach Number 4.15 and High Reynolds Numbers, " NASA TN D-2020, 1964.

[19] Bushnell, D. M., " Interference Heating on a Swept Cylinder in Region of Intersection with a Wedge at Mach Number 8, " NASA TN D-3094, 1965.

[20] Glass, C. E., Wieting, A. R., and Holden, M. S., " Effect of leading Edge Sweep on shock-shock interference at Mach 8, " AIAA Paper 89-0271, January 1989.

[21] Holst, T. L., Tannehill, J. C., and Rakich, J. V., " Numerical Computation of Viscous Blunt Body Flows with Planer Impinging Shock," Presented at the NASA Conference on Aerodynamic Analysis Requiring Advanced Computers, March 4-6, 1975, Langley Research Center, Hampton, Virginia.

[22] Thomas, J. L. and Walters, R. W., " Upwind Relaxation Algorithms for the Navier-Stokes Equations, " AIAA Paper 85-1501, July 1985.

[23] Beam, R. M. and Warming, R. F.."An Implicit Factored Scheme for the Compressible Navier Stokes Equation,"AIAA Journal, Vol. 16, 1978, pp.393-401.

[24] Rumsey, C. L., Taylor, S. L., Thomas, J. L., and Anderson, W. K., " Application of an Upwind Navier-Stokes Code to a Two - Dimensional Transonic Airfoil Flow, " AIAA Paper 87-0413, January 1987.

[25] Abolhassani, J. S., Smith, R. E., and Tiwari, S. N., " Grid Adaption for Hypersonic Flow, " AIAA Paper 87-1169, June 1987.

[26] Singh, D. J., Kumar, A., and, Tiwari, S. N.,"Three-Dimensional Shock-Shock Interaction on the Scramjet Inlet," AIAA 90-0529, January 1990.

Table 1: Freestream conditions.

M_∞	Re_D	T_w/T_∞	Rn	δ	Type of Interaction
8.03	387500	2.382	0.076	12.5	IV (2D)
5.94	186000	6.857	0.025	15.0	IV (2D)
5.94	180000	6.611	0.025	10.0	V (3D)

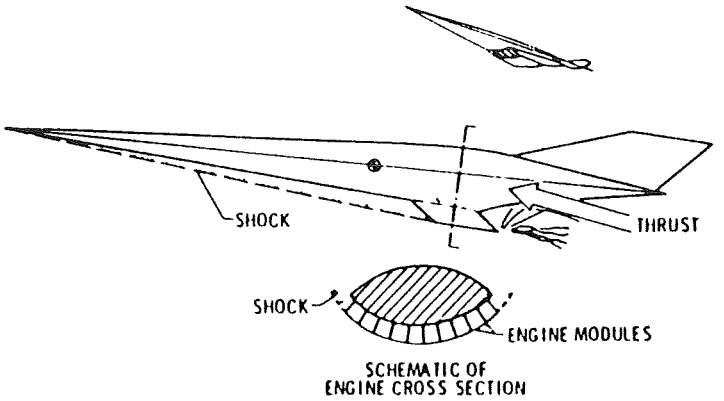

Figure 1: Airframe-integrated scramjet-engine concept.

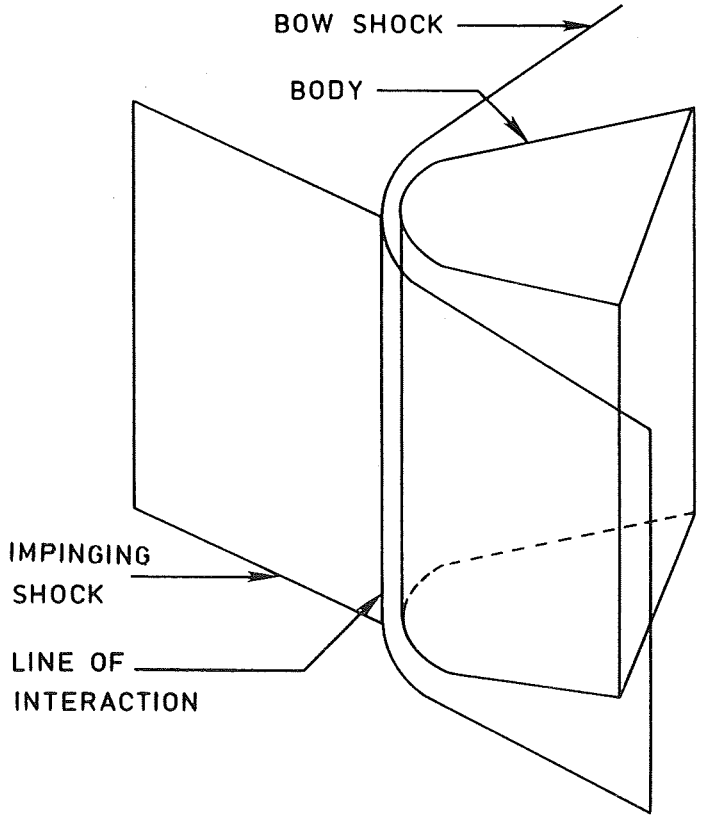

Figure 2: Physical model for shock-shock interaction on the topwall compression inlet (2D).

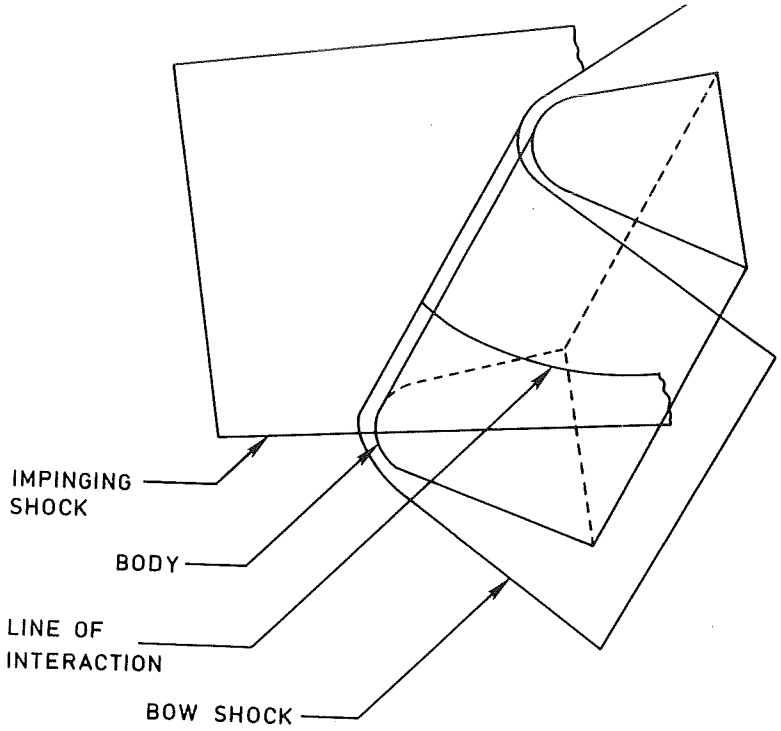

Figure 3: Physical model for shock-shock interaction on the sidewall compression inlet (3D).

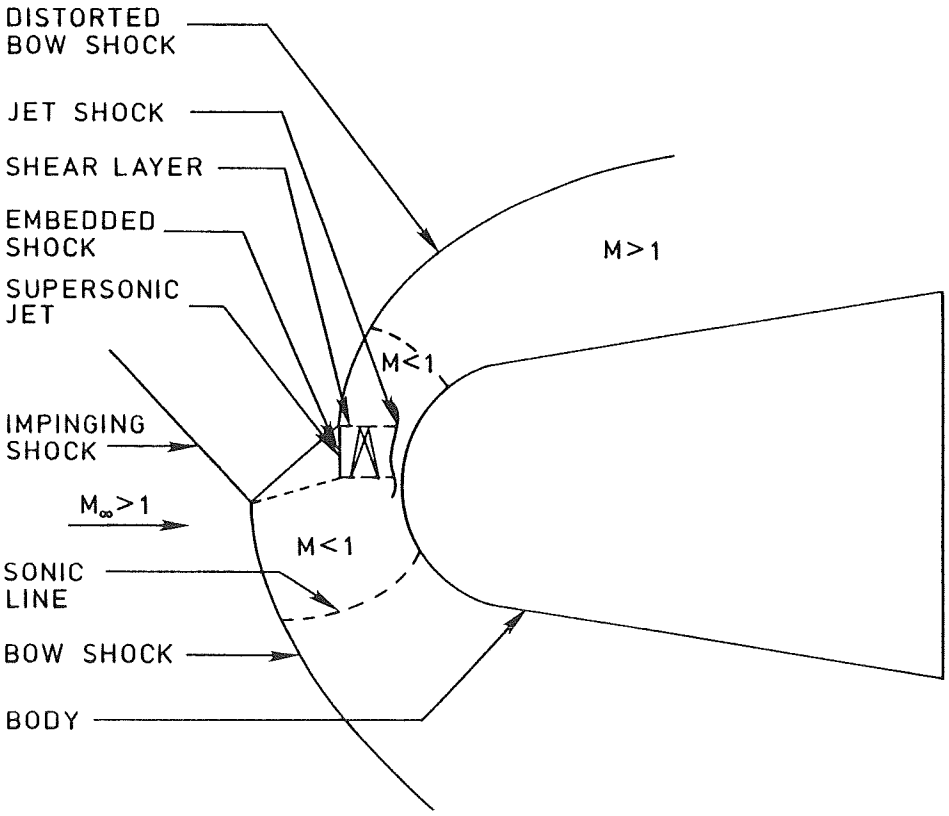

Figure 4: Schematic diagram for the Type IV interaction on the cowl.

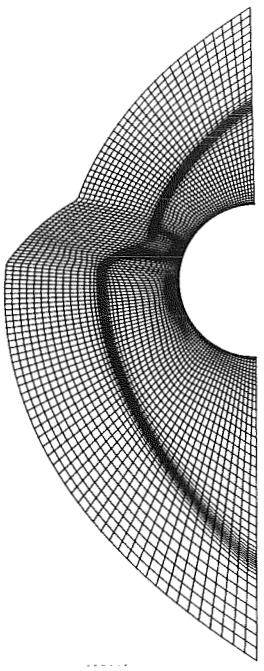

Figure 5: Cowl forebody grid for Mach 8.03 computations (adapted).

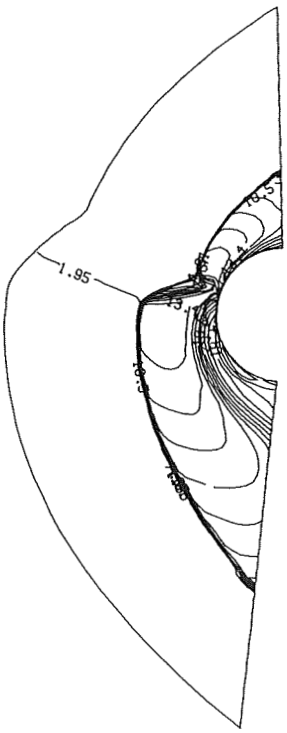

Figure 6: Temperature contours for the cowl forebody, $M_\infty = 8.03$.

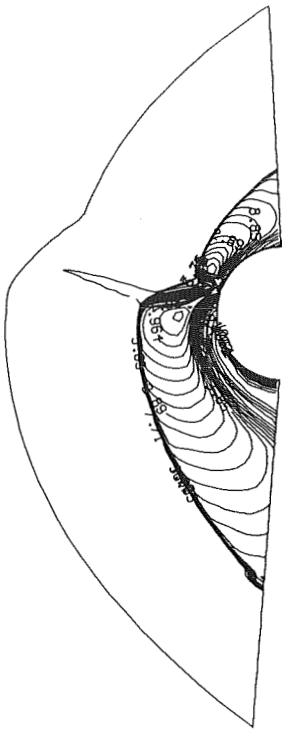

Figure 7: Mach number contours for the cowl forebody , $M_\infty = 8.03$.

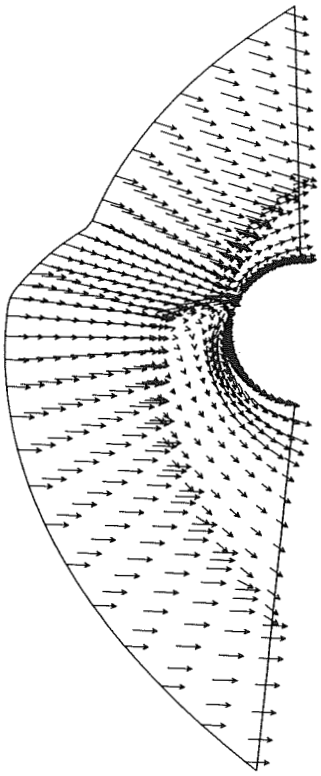

Figure 8: Velocity vectors for the cowl forebody, $M_\infty = 8.03$ with adapted grid.

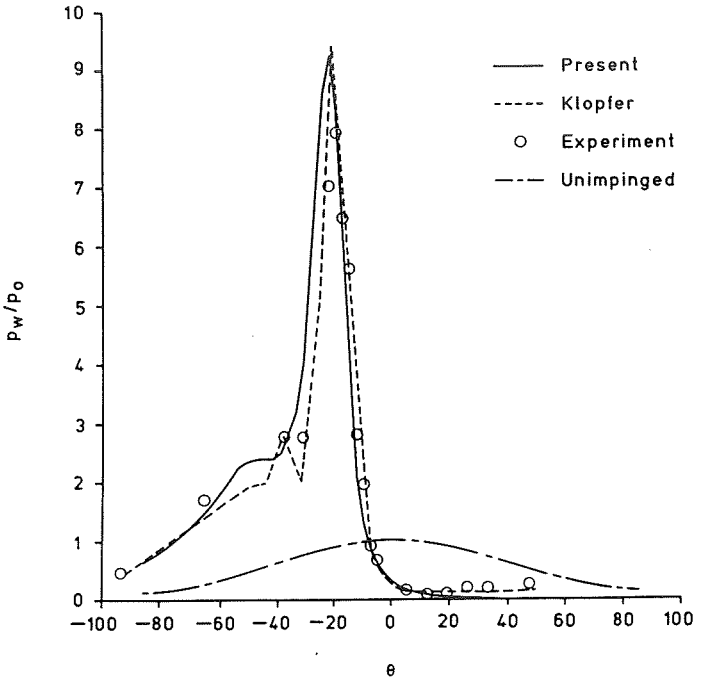

Figure 9: Variation of surface pressure for the cowl forebody, $M_\infty = 8.03$.

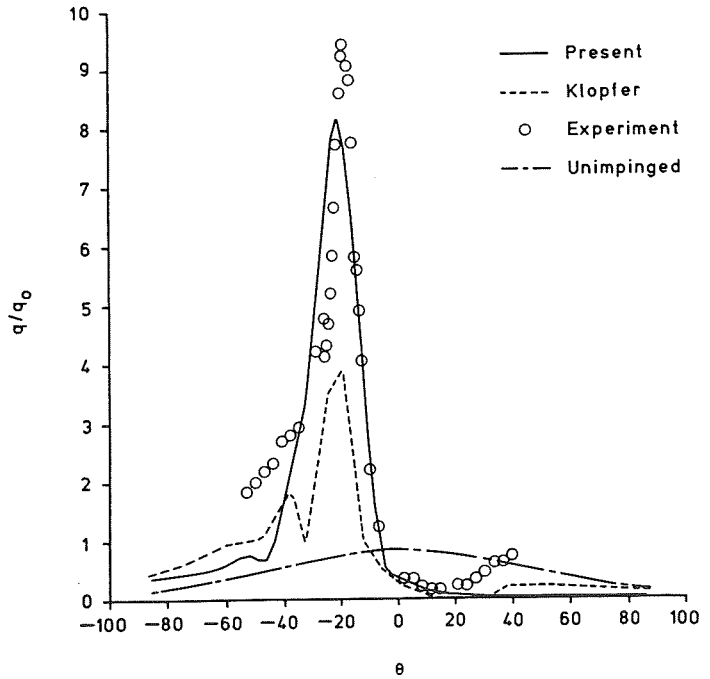

Figure 10: Variation of surface heat transfer for the cowl forebody, $M_\infty = 8.03$.

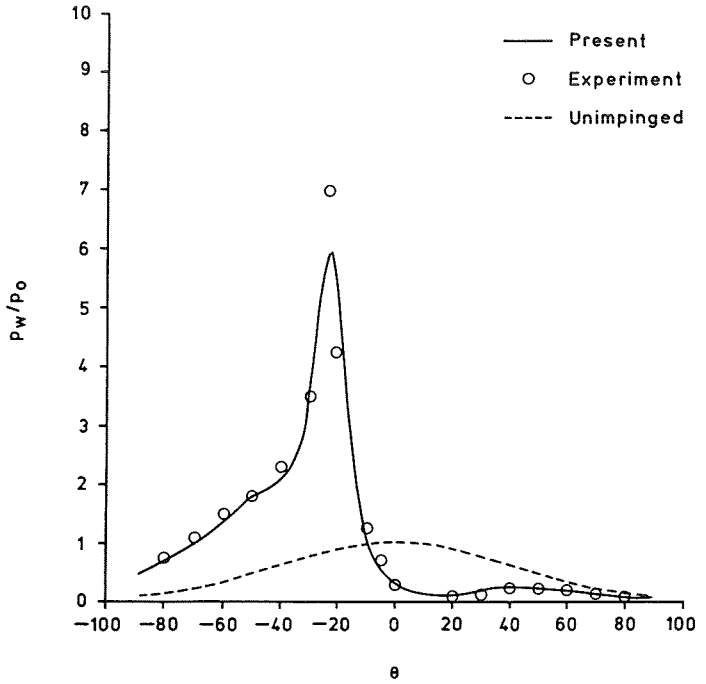

Figure 11: Variation of surface pressure for the cowl forebody, $M_\infty = 5.94$

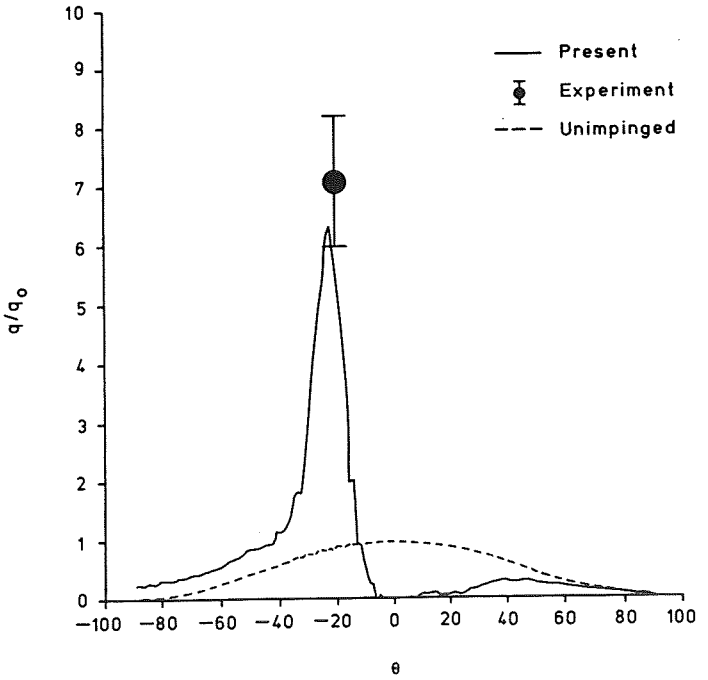

Figure 12: Variation of surface heat transfer for the cowl forebody, $M_\infty = 5.94$.

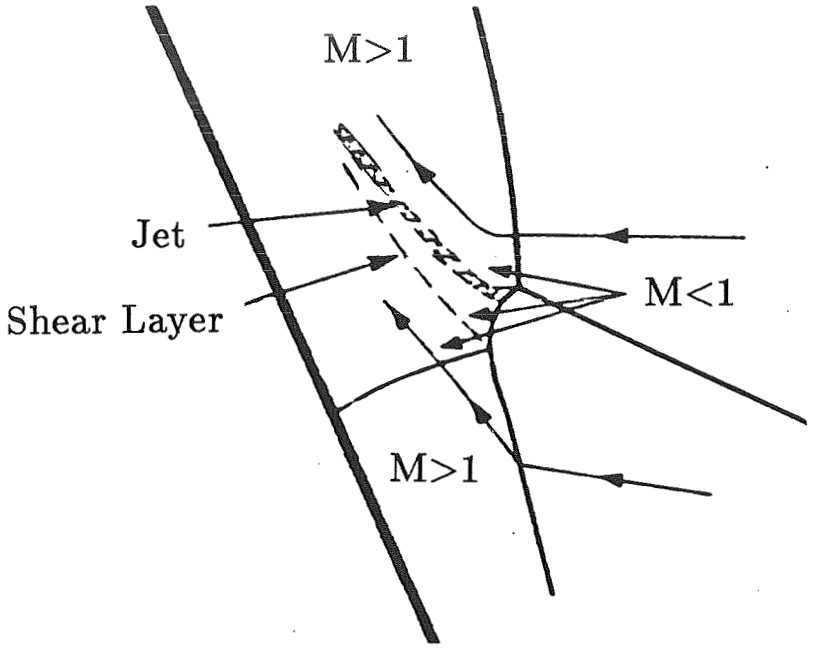

Figure 13: Schematic diagram for Type V interaction on the swept sidewall.

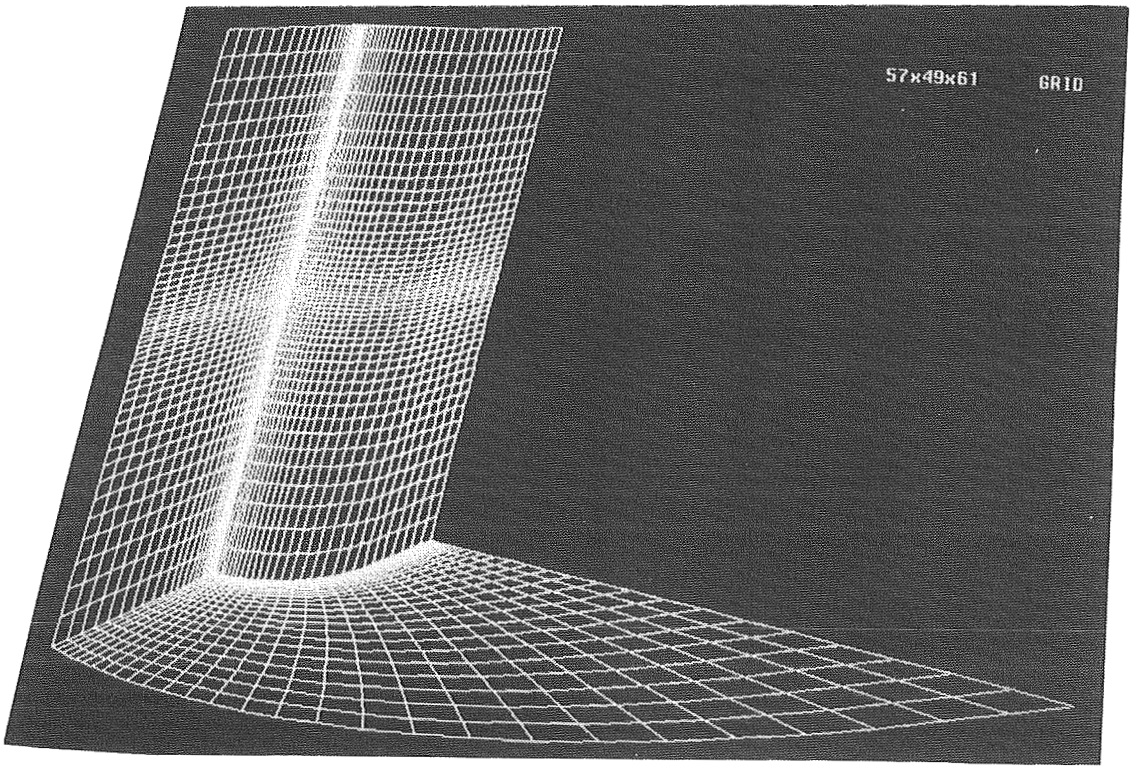

Figure 14: Grid distribution on the inlet sidewall.

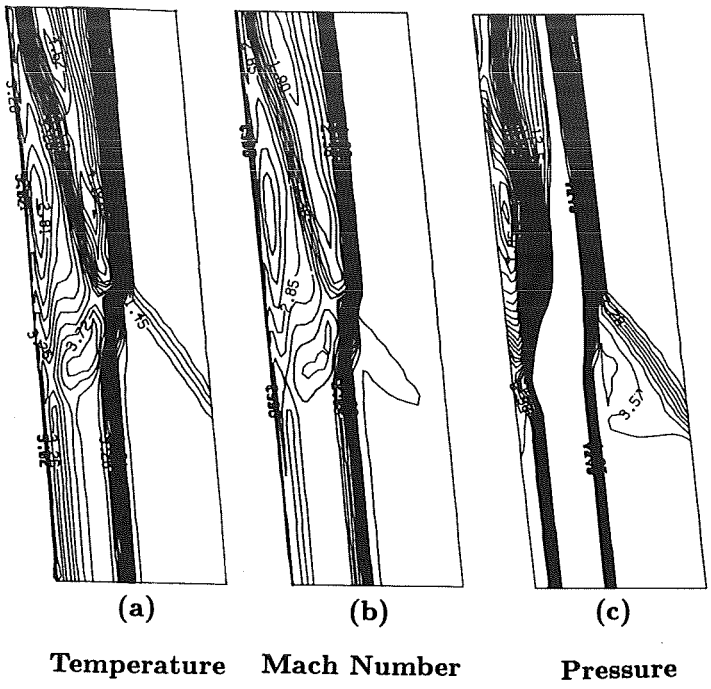

Figure 15: Temperature, Mach number and Pressure contours in the stagnation plane.

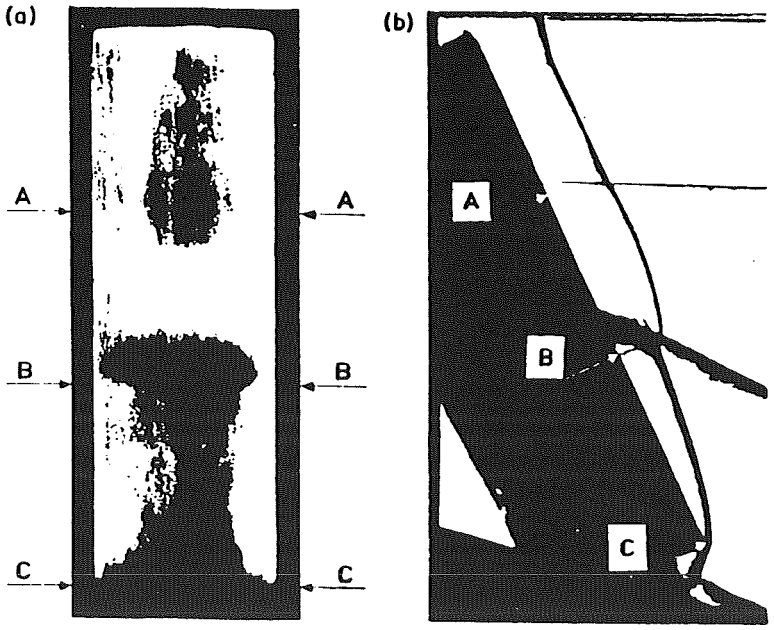

Figure 16: Local regions of high heating rates and corresponding schliern photograph (Ref. 1).

Figure 17: Surface pressure contours on the inlet sidewall.

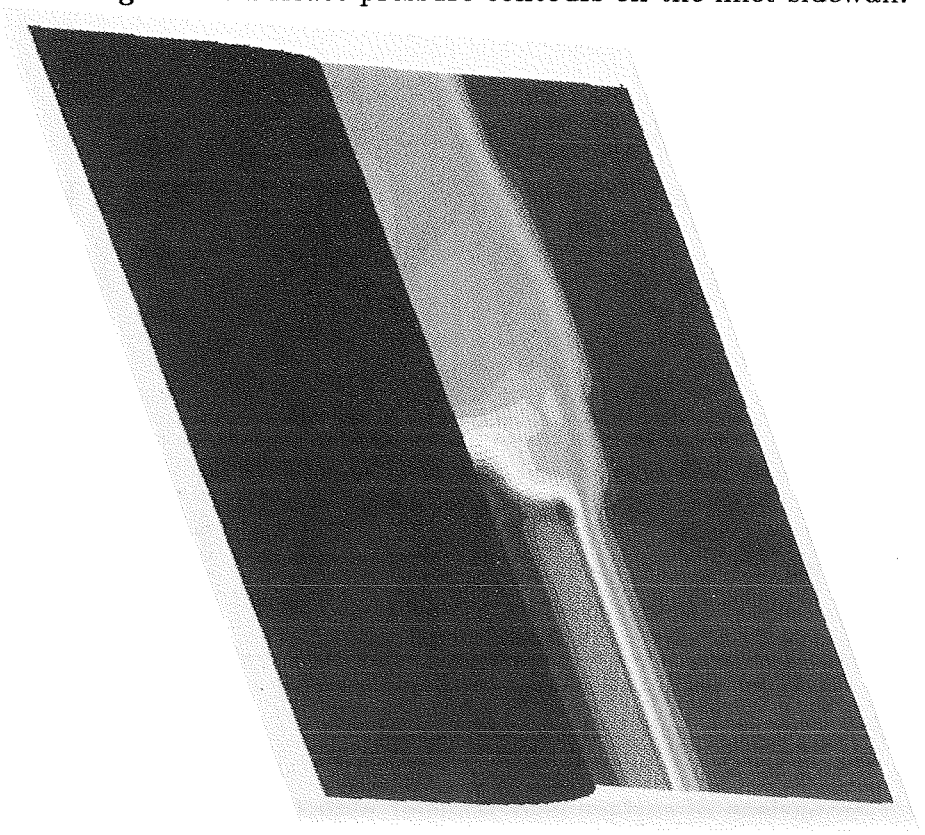

Figure 18: Pressure contours in the stagnation plane.

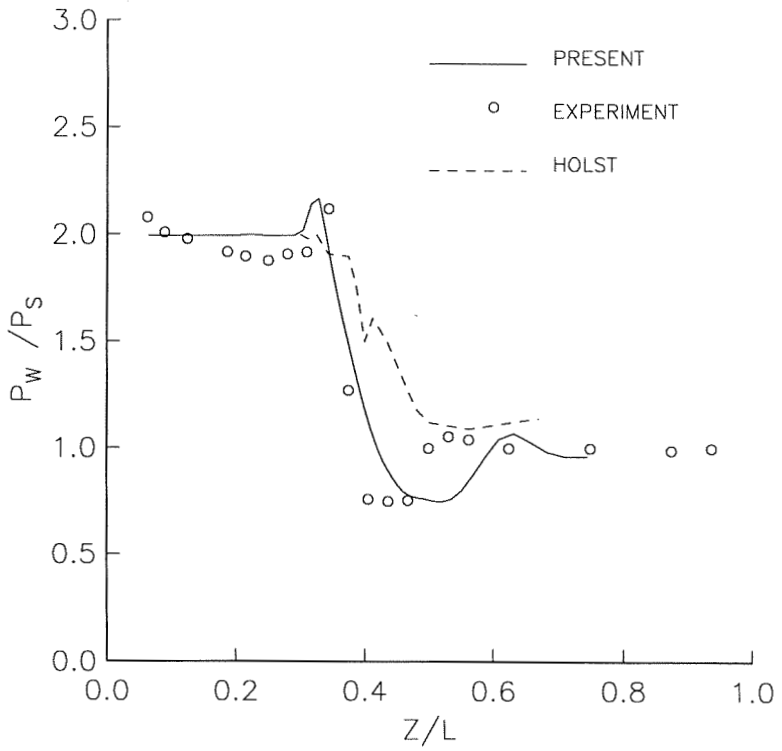

Figure 19: Comparison of surface pressure with the experimental data.

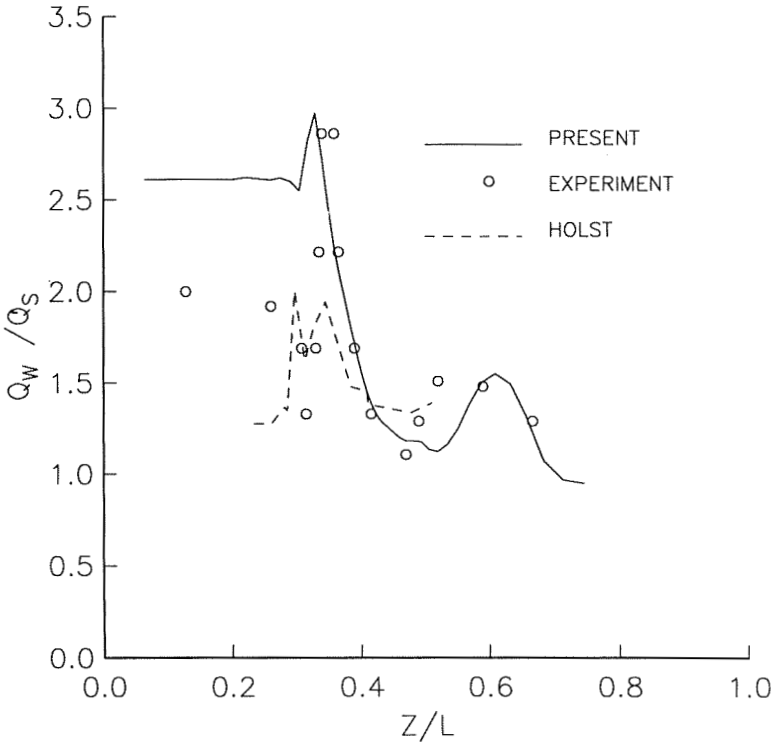

Figure 20: Comparison of surface heat transfer with the experimental data.